On the Significance of Two-Way Coupling in Simulation of Turbulent Particle Agglomeration

Farzad F. Dizaji and Jeffrey S. Marshall

Department of Mechanical Engineering, The University of Vermont,
Burlington, VT 05405, U.S.A.

Corresponding Author: Jeffrey S. Marshall, Department of Mechanical Engineering, The University of Vermont, Burlington, VT 05405, U.S.A. PHONE: 1 (802) 656-3826, EMAIL: jmarsha1@uvm.edu.

Abstract

A study is reported that examines computations of turbulent particle agglomeration with one-way and two-way phase coupling for cases with small overall particle concentration. The fluid flow was computed using a direct numerical computation using the point-force approximation for particle-induced body force, and a soft-sphere, adhesive discrete-element method was used to simulate the particulate transport and agglomerate formation. Computations were performed with different values of the Stokes number and the adhesion parameter. A variety of measures were used to examine both the effect of particle agglomeration on the fluid turbulence and the structure and flow field within the particle agglomerates. It was found that agglomeration has little influence on the attenuation of turbulence by the particles, at least in the range of Stokes numbers examined in the paper. Computations with two-way coupling generated agglomerates that were larger and contained more particles than those for one-way coupling. The agglomerate structure for both one-way and two-way coupling cases had a fractal structure with a similar value of the fractal dimension. As the agglomerate size increased, the fluid motion inside the agglomerates was found to become increasingly correlated to the agglomerate velocity, acting to decrease the relative velocity and shear stress of the inner particles within the agglomerate.

Keywords: particle agglomeration; collisions; turbulence modulation; fractal structure; turbulent agglomeration

1. Introduction

Particle agglomeration by fluid turbulence occurs in a large range of natural flow problems and industrial processes. Examples of natural processes include dispersion of atmospheric particulates, sediment transport and deposition in estuaries, removal of pollutants by sediment deposition in aquatic systems, particle transport from volcanic plumes, and agglomeration of ice crystals in the atmosphere during formation of snowflakes. The number of industrial processes involving turbulent agglomeration is immense, a few examples being fine particle separation in gas cyclones, wastewater treatment, additive manufacturing processes, flame synthesis of nanoparticles, and ash capture from combustion furnaces. Many industrial products are produced from powders or by precipitation from reactive solutions, examples including 3D printing, ceramic materials, catalysts, and many pharmaceutical products.

Numerous experimental studies have shown that the number of particles in an agglomerate tends to vary as a power-law function of the agglomerate size (e.g., as represented by the gyration radius), where the exponent of this power law (known as the fractal dimensional of the agglomerate group) is typically less than the dimension of the three-dimensional space in which the agglomerate is contained [1-3]. As a consequence, the average void fraction of the agglomerate increases as the number of particles within the agglomerate increases [4]. The value of the fractal dimension depends on the process by which the agglomerate was formed as well as the stage of the formation process. Typical values range from about 1.5 - 3.0 [5]. The effective mechanical properties of the agglomerate, such as the shear and elastic moduli, depend on the fractal dimension [6-8]. The fractal structure of the agglomerate also influences the density of force chains, which affects the shear stress necessary to induce agglomerate breakup and erosion [9-13].

Much of the theoretical and computational literature on turbulent agglomeration deals with the beginning stage of agglomeration, in which agglomerates are growing in size by collision of particles and of smaller agglomerates [14-19]. This literature uses several important approximations, including the approximation that two colliding particles will stick together, the approximation that an agglomerate can be represented by an equivalent spherical particle, and the approximation that the fluid turbulence is unaffected by the particle agglomeration process (one-way coupling). The particle collisions are typically assumed to be controlled by shear stress at the Kolmogorov scale, and various stochastic theories are used to model the particle collision rate, some of which (but not all) additionally assume small Stokes numbers. An experimental test of some of these stochastic collision rate theories was presented by Duru et al. [20] for aerosol droplets in oscillating grid turbulence. The experimental values were observed to be between 50-100% larger than the theoretical predictions of Chun and Koch [17], and in typical experiments the mean droplet size increased by about 3% during the experiment. A direct numerical simulation of the early stages of particle agglomeration was given by Reade and Collins [21], which again uses the equivalent sphere approximation and examines how the size distribution of the equivalent spheres varies with Stokes number.

There is an extensive literature examining the effect of particles on fluid turbulence. Reviews were given by Crowe [22], Eaton [23], Saber et al. [24], Poelma and Ooms [25], Rao et al. [26] and Balachandar and Eaton [27]. While most work has focused on turbulence modulation by relatively dilute particulate suspensions, Nasr and Ahmadi [28] demonstrated the importance of including particle collisions in modeling particle effects on fluid turbulence. However, there is almost no research to date on the effect of particle agglomeration on turbulent flows. While one might proceed by employing the equivalent sphere approximation for the particle agglomerates

and using existing literature for turbulence modulation from suspensions of individual particles, such an approach would neglect a number of fundamental physical aspects of particle agglomeration. Due to the fractal structure of turbulent agglomeration, the particle volume fraction within agglomerates varies strongly as a function of agglomerate size, which in turn has a strong influence on the effective particle mass and the properties controlling agglomerate deformation and breakup [6, 7, 8, 10, 11, 29] which would not be accurately represented by a set of equivalent spheres with uniform properties. Particle agglomerates are porous to various degrees, and depending on the agglomerate size and structure the flow through an agglomerate can have a significant effect on agglomerate response to turbulent fluctuations and to collisions with other agglomerates [30, 31]. Particle agglomerates are typically not spherical, but can be elongated or even have a convoluted structure with various branches. Finally, the bonds holding particles into an agglomerate can break, either due to fluid forces and due to collisions with other agglomerates, which might cause a gradual erosion of particles from the agglomerate or a sudden rupture of the agglomerate into some number of offspring agglomerates [12, 13, 32].

The current paper presents a computational study of turbulent agglomeration that resolves the individual agglomerate particles and their interactions with surrounding particles. Since we do not invoke the approximation of treating the agglomerates as equivalent spheres, as used in previous research, important phenomena such as agglomerate permeability [30] and breakup [13] were included in the simulations without the need to introduce additional phenomenological models. A particular objective of the current paper is to examine the significance of two-way coupling on the turbulent agglomeration process, which was done by comparing results of computations performed with two-way coupling to those of computations conducted with one-way coupling, and by examining the flow field around the agglomerate structures that give rise to

differences between the one-way and two-way coupling results. The computations were performed using a soft-sphere discrete element method (DEM) for adhesive particles subject to van der Waals adhesion [33], and the fluid flow computations were performed using a pseudo-spectral method to simulate forced turbulence in a triply-periodic domain. The two-way coupling effect of particle forces on the fluid flow was accounted for using an effective body force in the fluid flow simulations, similar to the approach used for simulation of sedimenting particle agglomerates by Bosse et al. [34]. The various computational methods used to simulate particle and fluid transport are summarized in Section 2, followed by results and discussion in Section 3. Section 3.1 examines the effect of turbulent agglomeration on modulation of the turbulence by the particulate phase. Section 3.2 examines various measures of agglomerate structure for cases with and without two-way coupling. Conclusions are given in Section 4.

2. Computational Methods

The computations of particle agglomeration were performed using an adhesive discrete element method (DEM) to model particle transport and collisions. Homogeneous turbulence was simulated using a forced pseudo-spectral direct numerical simulation (DNS) method on a triply-periodic domain. Each of these methods has been described in detail elsewhere, but the key points and appropriate references are summarized below.

2.1. Discrete Element Method (DEM) for Particle Transport

The discrete-element method (DEM) of Marshall [33] was used to transport adhesive particles in the turbulent flow. The computational method uses a multiple time step algorithm, in which the fluid time step $\Delta t = O(\ell / u_0)$, the particle time step $\Delta t_p = O(d / u_0)$, and the collision

time step $\Delta t_c = O(d(\rho_p^2 / E_p^2 u_0)^{1/5})$ satisfy $\Delta t > \Delta t_p > \Delta t_c$. Here d is the particle diameter, ρ_p is the particle density, and E_p is the particle elastic modulus. The method follows the motion of individual particles in the three-dimensional fluid flow by solution of the particle momentum and angular momentum equations

$$m\frac{d\mathbf{v}}{dt} = \mathbf{F}_F + \mathbf{F}_A, \qquad I\frac{d\boldsymbol{\Omega}}{dt} = \mathbf{M}_F + \mathbf{M}_A, \tag{5}$$

subject to forces and torques induced by the fluid flow ($\mathbf{F}_F$ and $\mathbf{M}_F$) and by the particle collision and adhesion ($\mathbf{F}_A$ and $\mathbf{M}_A$). Here, m is the particle mass, I is the moment of inertia, and $\mathbf{v}$ and $\boldsymbol{\Omega}$ are the particle velocity and rotation rate, respectively. The dominant fluid force is the drag force, which is given by the Stokes drag law modified to account for the effect of local particle crowding as

$$F_d = 3\pi\mu d(\mathbf{u} - \mathbf{v})f, \tag{6}$$

where $\mathbf{u}$ is the fluid velocity evaluated at the particle centroid. The friction factor f was given empirically by Di Felice [35] for particle Reynolds numbers $\mathrm{Re}_p \equiv |\mathbf{u} - \mathbf{v}|d/\nu$ in the range 0.01 to 10^4 as a function of the local particle volume fraction ϕ as

$$f = (1-\phi)^{1-\zeta}, \qquad \zeta = 3.7 - 0.65\exp\left(-\frac{1}{2}[1.5 - \ln(\mathrm{Re}_p)]^2\right). \tag{7}$$

This expression approaches the Wen and Yu [36] expression for low particle Reynolds number. The associated viscous fluid torque arises from a difference in rotation rate of the particle and the local fluid element, and was given by [37] as

$$\mathbf{M}_F = -\pi\mu d^3(\mathbf{\Omega} - \frac{1}{2}\boldsymbol{\omega}), \tag{8}$$

where $\boldsymbol{\omega}$ is the fluid vorticity vector at the particle centroid. Other fluid forces of lesser importance accounted for in the computation include the Saffman and Magnus lift terms [38-39], which together with drag make up the fluid force $\mathbf{F}_F$.

The total collision and adhesion force and torque fields on particle *i* with radius r_i are given by

$$\mathbf{F}_A = -F_n\mathbf{n} + F_s\mathbf{t}_S, \qquad \mathbf{M}_A = rF_s(\mathbf{n}\times\mathbf{t}_S) + M_r(\mathbf{t}_R\times\mathbf{n}) + M_t\mathbf{n}, \tag{9}$$

where $\mathbf{n} = (\mathbf{x}_j - \mathbf{x}_i)/|\mathbf{x}_j - \mathbf{x}_i|$ is the unit normal vector oriented along the line connecting the centers of the two colliding particles, *i* and *j*. The normal component of the collision and adhesion force F_n is further divided into an elastic-adhesion part F_{ne} and a dissipative part F_{nd}. The sliding resistance is composed of a force with magnitude F_s acting in a direction $\mathbf{t}_S$, corresponding to the direction of relative motion of the particle surfaces at the contact point projected onto the contact plane (the plane orthogonal to **n**), as well as a related torque in the $\mathbf{n}\times\mathbf{t}_S$ direction. The rolling resistance, which arises due to the effects of particle adhesion, exerts a torque of magnitude M_r on the particle in the $\mathbf{t}_R\times\mathbf{n}$ direction, where $\mathbf{t}_R$ is the

direction of the "rolling" velocity. The twisting resistance torque M_t is oriented along the unit normal direction **n**. While all of these various collision-adhesion forces and torques were included in the current computations, the dynamics of small adhesive particles are dominated by the normal elastic-adhesive force and the rolling resistance torque.

The adhesive force between the two particles depends on the surface energy potential γ, where the work required to separate two spheres colliding over a contact region of radius $a(t)$ is given by $2\pi\gamma a^2$ in the absence of further elastic deformation. Particle normal elastic rebound force and adhesion force were simulated by employing the soft-sphere collision model of Johnson et al. [40], hereinafter referred to as the JKR model, which can be written in terms of the contact region radius $a(t)$ and the normal particle overlap $\delta_N = r_i + r_j - \left|\mathbf{x}_i - \mathbf{x}_j\right|$ as [41]

$$\frac{\delta_N}{\delta_c} = 6^{1/3}\left[2\left(\frac{a}{a_o}\right)^2 - \frac{4}{3}\left(\frac{a}{a_o}\right)^{1/2}\right], \qquad \frac{F_{ne}}{F_c} = 4\left(\frac{a}{a_o}\right)^3 - 4\left(\frac{a}{a_o}\right)^{3/2}, \tag{10}$$

The critical overlap δ_c, the critical normal force F_c, and the equilibrium contact region radius a_o are given by [40]

$$F_c = 3\pi\gamma R, \qquad \delta_c = \frac{a_o^2}{2(6)^{1/3}R}, \qquad a_o = \left(\frac{9\pi\gamma R^2}{E}\right)^{1/3}. \tag{11}$$

As two particles move away from each other following collision, they remain in contact until the point where $F_n = -F_c$ and $\delta_N = -\delta_c$ due to the necking of the material in the contact region. Beyond this state any further separation leads the two particles to break apart.

The effect of the fluid squeeze-film within the contact region is to limit the minimum approach distance between the particles (i.e., the contact region gap size) and to reduce the particle restitution coefficient. Experimental studies of particle collisions at different Stokes numbers [42] indicate that the coefficient of restitution is essentially zero when the Stokes number is less than about 10 due to dissipation in the squeeze-film. Since our Stokes numbers are well below this value, we set the dissipative part of the normal collision force F_{nd} such that the restitution coefficient vanishes using the model of Tsuji et al. [43].

The second major effect of particle adhesion is to introduce a torque that resists particle rolling. For uniform-size spherical particles, the "rolling velocity" $\mathbf{v}_L$ of particle *i* is given by [44]

$$\mathbf{v}_L = -R(\boldsymbol{\Omega}_i - \boldsymbol{\Omega}_j) \times \mathbf{n} \ . \tag{12}$$

A linear expression for the rolling resistance torque M_r was postulated as

$$M_r = -k_R \, \xi \, , \tag{13}$$

where $\xi = (\int_{t_0}^{t} \mathbf{v}_L(\tau) \, d\tau) \cdot \mathbf{t}_R$ is the rolling displacement in the direction $\mathbf{t}_R = \mathbf{v}_L / |\mathbf{v}_L|$. Rolling involves an upward motion of the particle surfaces within one part of the contact region and a

downward motion in the other part of the contact region. The presence of an adhesion force between the two contacting surfaces introduces a torque resisting rolling of the particles. An expression for the rolling resistance due to van der Waals adhesion was derived by Dominik and Tielens [45], which yields the coefficient k_R as

$$k_R = 4F_C(a/a_0)^{3/2}. \tag{14}$$

Dominik and Tielens [45] further argue that the critical resistance occurs when the rolling displacement ξ achieves a critical value, corresponding to a critical rolling angle $\theta_{crit} = \xi_{crit}/R$. For $\xi > \xi_{crit}$, the rolling displacement ξ in (13) is replaced by ξ_{crit}. The expressions used for twisting and sliding resistances are given by Marshall [33].

2.2. Direct Numerical Simulation (DNS) of Homogeneous Turbulence

The DNS computations of isotropic, homogeneous turbulence used for validation were performed using a triply-periodic pseudo-spectral method with second-order Adams-Bashforth time stepping and exact integration of the viscous term [46]. In this approach, the spectral Navier-Stokes equations are evolved in time after having been projected onto a divergence-free space using the operator $P_{ij} = k_i k_j / k^2 - \delta_{ij}$ according to the expression

$$\overline{\mathbf{u}}^{n+1} = \overline{\mathbf{u}}^{n} \exp(-\nu k^2 \Delta t) + \Delta t\, \mathbf{P} \cdot \left[\frac{3}{2} \overline{\mathbf{F}}^{n} \exp(-\nu k^2 \Delta t) - \frac{1}{2} \overline{\mathbf{F}}^{n-1} \exp(-2\nu k^2 \Delta t) \right], \tag{15}$$

where an overbar denotes Fourier transform in three space dimensions, a superscript indicates the time step, ν is the kinematic viscosity, and **k** is the wavenumber vector with magnitude *k*. The force vector **F** on the right-hand side has Fourier transform given by

$$\overline{\mathbf{F}} = \overline{\mathbf{u} \times \boldsymbol{\omega}} + \bar{\mathbf{f}}_F + \bar{\mathbf{f}}_P , \tag{16}$$

where $\bar{\mathbf{f}}_F$ is the small wavenumber forcing term required to maintain the turbulence with approximately constant kinetic energy and $\bar{\mathbf{f}}_P$ is the particle-induced body force due to relative motion between the particles and the fluid. The velocity field was made divergence-free at each time step by taking its Fourier transform and using the spectral form of the continuity equation, given by

$$\mathbf{k} \cdot \overline{\mathbf{u}} = 0 . \tag{17}$$

The forcing vector was assumed to be proportional to the fluid velocity [47-48], such that

$$\bar{\mathbf{f}}_F = \begin{cases} C\overline{\mathbf{u}} & \text{for } k < k_{crit} \\ 0 & \text{for } k > k_{crit} \end{cases} , \tag{18}$$

where the coefficient *C* was set equal to $C = 0.0045 / E_{low}$ and $E_{low} = \frac{1}{2} \sum_{k<k_{crit}} \overline{\mathbf{u}} \cdot \overline{\mathbf{u}}$ is the kinetic energy in all modes with wavenumber amplitude $k < k_{crit}$. The current computations were performed with $k_{crit} = 5$, so that the forcing acts only on the large-scale eddies.

The particle body force $\mathbf{f}_P$ was computed by associating a regularized delta function $\delta_h(\mathbf{x}-\mathbf{X}_n)$ with each Lagrangian particle, where $\mathbf{X}_n$ denotes the particle centroid location of particle *n*. The value of the body force $\mathbf{f}_P$ was evaluated at each grid node *i* of the Cartesian grid using

$$\mathbf{f}_p(\mathbf{x}_i) = -\sum_{n=1}^{N} \mathbf{F}_{F,n}\, \delta_h(\mathbf{x}_i - \mathbf{X}_n)\,, \tag{19}$$

where $\mathbf{F}_{F,n}$ denotes the fluid force on the n^{th} particle. The regularized delta function used for the current problem distributes the particle force uniformly over a stencil consisting of the grid cell containing the particle and one grid cell on each side. This choice of delta function is conservative in both the force and torque for any value of $\mathbf{X}_n$.

The turbulence kinetic energy *q* and dissipation rate ε were obtained from the power spectrum, $e(k)$, as

$$q = \int_0^{k_{\max}} e(k)dk\,, \qquad \varepsilon = 2\nu\int_0^{k_{\max}} k^2 e(k)dk\,. \tag{20}$$

Various dimensionless measures describing the turbulence in the validation computations are listed in Table 1, including the root-mean-square velocity magnitude u_0, the average turbulence kinetic energy *q*, the integral length scale $\ell_0 = 0.5\, u_0^{\,3}/\varepsilon$, the Taylor microscale $\lambda = (15\nu/\varepsilon)^{1/2} u_0$, and the Kolmogorov length scale $\eta = (\nu^3/\varepsilon)^{1/4}$. The corresponding microscale Reynolds number is $\mathrm{Re}_\lambda = u_0\lambda/\nu = 99$.

2.3. Dimensionless Parameters

One of the most important dimensionless parameters is the Stokes number, which is defined as the ratio of the particle time scale $\tau_p = m/3\pi\mu d$ to a characteristic fluid time scale, where m is the particle mass. For turbulent flow, different Stokes numbers can be defined using different fluid time scales. Two common choices are the Kolmogorov-scale Stokes number St_K and the integral-scale Stokes number St_0, defined by

$$\mathrm{St}_K = \tau_p / \tau_\eta, \qquad \mathrm{St}_0 = \tau_p / \tau_\ell. \tag{21}$$

The Kolmogorov time scale τ_η is defined in terms of the kinematic viscosity and turbulence dissipation rate as $\tau_\eta = (\nu/\varepsilon)^{1/2}$ and the integral time scale is given by $\tau_\ell = \ell_0 / u_0$. The Stokes number determines the particle response to changes in the fluid flow, such that in cases with small Stokes numbers particles nearly follow fluid streamlines and in cases with large Stokes numbers the fluid has only a small influence on the particle motion.

The tendency for colliding particles to adhere to each other can be characterized by the adhesion parameter Ad, defined in terms of the adhesive surface energy density γ as [49]

$$\mathrm{Ad} = \frac{2\gamma}{\rho_p U^2 d}. \tag{22}$$

In this equation, U is a characteristic velocity scale of the fluid, which might be set equal to the root-mean-square turbulent fluctuation velocity u_0 to obtain the integral-scale adhesion parameter Ad_0 or to the Kolmogorov velocity $u_\eta = (\nu\varepsilon)^{1/4}$ to obtain the Kolmogorov-scale adhesion parameter Ad_K. The adhesive energy density γ can be related to the Hamaker coefficient A for the particle material operating in the given fluid medium by

$$\gamma = \frac{A}{24\pi\delta^2}, \tag{23}$$

where δ is the gap thickness within the contact area.

The elastic rebound force on the particle is characterized using an elasticity parameter El, defined by

$$\mathrm{El} = \frac{E}{\rho_p U^2}, \tag{24}$$

where E is the effective elastic modulus, which together with the effective particle radius R is defined by

$$\frac{1}{E} \equiv \frac{1-\sigma_i^2}{E_i} + \frac{1-\sigma_j^2}{E_j}, \qquad \frac{1}{R} \equiv \frac{1}{r_i} + \frac{1}{r_j}, \tag{25}$$

where E_i, σ_i, and r_i are the elastic modulus, Poisson ratio, and radius of particle i, respectively. Both the elasticity parameter El and the adhesion parameter Ad are important in determining the

radius of the contact region upon particle collision. In (23), the fluid velocity scale U may again be modeled using either the integral scale (root-mean-square) velocity u_0 or the Kolmogorov-scale velocity u_η.

3. Results and Discussion

The computations were initialized by positioning 46,656 particles on a uniform array across the computational domain. A preliminary computation was conducted with no particles to allow the turbulence to develop a range of length scales characteristic of statistically stationary homogeneous isotropic turbulence. The computation was then restarted with particles using the three-level multiple time-step DEM algorithm of Marshall [33], with a fluid time step of $dt_f = 0.005$, 10 particle time steps per fluid time step, and 40 collision time steps per particle time step. A listing of the parameter values for the different runs with particles is given in Table 2, where the different runs are referred to in the following as case 1-12.

3.1. Effect of Particle Agglomeration on Turbulence

The turbulent kinetic energy q and turbulent dissipation rate ε are plotted as functions of time for cases with both one-way and two-way coupling in Figure 1 for case 2. For the one-way coupling computations, both q and ε fluctuate in time with root-mean-square values of 4.6% and 7.5% of their mean values, respectively. The computations with two-way coupling result in values of turbulent kinetic energy that exhibit fluctuations with a similar root-mean-square value up to about $t \approx 87$, after which the kinetic energy decreases sharply. The turbulent dissipation for the two-way coupling computation is observed to decrease to about 20% below the average value for the one-way coupling simulation up to a time of about $t \approx 60$, after which the dissipation rate

in the two-way coupling computation decreases steadily. We note that the dissipation rate measure ε reported here is due to fluid gradients, and it does not include the dissipation caused by the particle drag force on the fluid.

A plot of the power spectrum at three different times is presented in Figure 2a, showing a gradual decrease in the spectrum with time for the case with two-way coupling. The power spectrum is nearly constant in time for the one-way coupling case. The $k^{-5/3}$ scaling of the power spectrum in the inertial range is indicated by a dashed line. A comparison of the power spectra for cases with different Stokes numbers is given in Figure 2b. The change in Stokes number in this figure was produced by changing the particle radius, with all other parameters held fixed. Two computations were conducted with each value of particle radius, one with adhesive particles (Ad_0 = 12.3, cases 1-4) and one with no adhesion (Ad_0 = 0, cases 5-8). The power spectra were plotted in Figure 2b at time $t = 87.5$, near the end of the runs and just before the turbulent kinetic energy decreases sharply. The power spectra curves for the case with lowest Stokes number (St_K = 0.86) are almost identical to the initial power spectrum, showing almost no change with the addition of the particles.

The cases with higher Stokes number exhibit progressively lower power spectra curves as the particle size is increased. It is noted that several different regimes characterizing turbulence modulation by particles have been noted in the literature. For very small particles with Kolmogorov-scale Stokes number St_K <<1, the particles are found to enhance the fluid inertia and hence increase the turbulent kinetic energy [50, 51]. For particles with larger Stokes number (St_K >>1) but with diameter d less than about 10% of the integral length scale ℓ_0, the particles reduce the turbulent kinetic energy. This reduction is generally associated with the preferential concentration of particles in regions of low fluid vorticity [52-55]. Druzhinin [51] reported the

transition between these two regimes to occur at $St_K \cong 0.8$. Finally, sufficiently large particles are again observed to enhance turbulent kinetic energy due to shedding of vortex structures in the particle wakes. Gore and Crowe [56] and Crowe [22] propose that this third regime corresponds to particles with diameter *d* satisfying $d / \ell_0 > 0.1$, but various other criteria have been suggested by other researchers. As seen from Tables 1 and 2, the current computations are clearly in this middle regime of turbulence modulation, and the observed enhanced attenuation of turbulent kinetic energy with increase in particle size and mass loading is consistent with the previous literature cited above for this regime.

The cases with the three smallest values of Stokes number in Figure 2b exhibit almost no difference in the power spectra between computations with and without adhesion. The case with largest Stokes number exhibits a reduction in the power spectrum for the case with adhesion compared to that with no adhesion. The fact that the power spectra shown in Figure 2b are so similar for the cases with and without adhesion, even though the curves exhibit significant decrease due to the presence of particles compared to the power spectrum for the one-way coupling computation, provides strong evidence that particle agglomeration has little influence on turbulence attenuation, at least for sufficiently small particles. This observation is consistent with the conclusion of Druzhinin [51] that the attenuation of turbulence by particles in this regime is primarily a consequence of the particle inertia, which depends only on net particle mass and is independent of agglomeration of the particles.

The size of the agglomerates that develop during the turbulent flow simulation depends upon the value of the adhesion parameter. As indicated in Table 2, the value of the adhesion parameter was varied in our computations over a factor of about 16. For significantly smaller values of adhesion parameter than those examined, there is only a small amount of particle

adhesion during the computational run time and the agglomerates are relatively small, with only 2-5 or so particles. For much larger values of adhesion parameter than those examined, the agglomerates grow to very large sizes during the computations, in some cases with all particles forming a single agglomerate. Our desire in this paper was to examine agglomerates that were sufficiently large (i.e., several hundred particles) so that measures such as fractal dimension are sensible, but also agglomerates whose maximum size was of the order of magnitude of the integral length scale of the turbulence. Figure 3a shows the average number of particles per agglomerate, N_{pagg}, at time $t = 87.5$ as a function of adhesion parameter. The agglomerate size can be estimated by the radius of gyration, R_{gyr}, defined for an agglomerate i by

$$R_{gyr,i} = \left[\frac{1}{N_i} \sum_{j=1}^{N_j} \left| \mathbf{x}_j - \overline{\mathbf{x}}_i \right|^2 \right]^{1/2}, \tag{26}$$

where $\overline{\mathbf{x}}_i$ denotes the centroid position of agglomerate i and $\mathbf{x}_j$ is the centroid position of the j^{th} particle within the agglomerate. The average value of the radius of gyration tends to be dominated by the smallest, but more numerous, agglomerates. Instead, we define a particle-weighted radius of gyration, $\overline{R}_{gry}$, by

$$\overline{R}_{gyr} = \frac{1}{N_{agg}} \sum_{i=1}^{N_{agg}} N_i R_{gry,i}, \tag{27}$$

where N_i is the number of particles in agglomerate i and N_{agg} is the total number of agglomerates. A plot of $\overline{R}_{gry} / r_p$, where r_p is the radius of a single particle, at time $t = 87.5$ is presented in Figure 3b as a function of adhesion parameter for both computations with one-way and two-way coupling.

3.2. Structure of Particle Agglomerates

This section examines the detailed structure of the particle agglomerates, as predicted using both one-way and two-way coupling simulations. This study was performed starting from a state in which no particles were touching, and hence there were no agglomerates, and ending at a time of $t = 87.5$. By this end time the agglomerates had developed into large structures, but they had not yet achieved an equilibrium condition where agglomerate breakup balances agglomerate formation by collision. This end time was selected because shortly after this time in the two-way coupling simulations, the turbulent kinetic energy decreases sharply, leading eventually to a state where the small-scale turbulence completely vanishes. On the other hand, at $t = 87.5$ the turbulent kinetic energy is still reasonably close to its initial value, as shown in Figure 1a.

Agglomerates are defined as groups of particles that are in contact with each other, either directly or via contacts with other particles. The agglomerates were identified at each time step of the computation and a variety of measures were employed to examine their characteristics. The total number of agglomerates N_{agg} is plotted as a function of time for case 2 in Figure 4a for computations with both one-way and two-way coupling of the particle and fluid phases. Shortly after the start of the computation, individual particles collide and attach to each other to form small agglomerates. A maximum in the number of agglomerates is reached at $t \cong 15$, equal to approximately 7400 agglomerates. The number of agglomerates then decreases as these small

agglomerates collide and adhere to each other to form larger agglomerates. The number of particles N_i in each agglomerate was counted and averaged over all agglomerates to obtain the average number of particles per agglomerate, which is plotted as a function of time in Figure 4b. The dimensionless particle-weighted radius of gyration, $\overline{R}_{gyr} / r_p$, is plotted as a function time in Figure 4c.

In all three of the plots in Figure 4, the one-way and two-way coupling results are quite close to each other for times near the beginning of the calculation. At $t \approx 20$ we notice that the radius of gyration in Figure 4c for the two-way coupling run increases above that for the one-way coupling run. The number of particles per agglomerate in Figure 4b similarly is greater for the two-way coupling run than it is for the case with one-way coupling; however, the differences between the one-way and two-way coupling runs appear later than for the radius of gyration. Since the agglomerates for two-way coupling are both larger and have more particles than for one-way coupling, it follows that the number of agglomerates shown in Figure 4a for the two-way coupling computation is less than that for one-way coupling, although again we see that this difference appears significantly later than in the plot of the radius of gyration.

As noted by a number of previous authors [1-3], the number of particles N_i in agglomerate *i* can be expressed as a power-law function of the agglomerate size, such that

$$N_i = K(R_{gyr,i} / r_p)^{d_f}, \tag{28}$$

where *K* is a coefficient (called the fractal pre-factor) and the exponent d_f is called the fractal dimension of the set of agglomerates. The value of d_f varies over the interval $1 \le d_f \le 3$

depending on the agglomeration formation mechanism [5]. For instance, Eggersdorfer et al. [57] cited typical values of $d_f = 2.5$ for diffusion-limited agglomeration, $d_f = 3.0$ for ballistic particle-cluster agglomeration, and $d_f = 1.8$ for diffusion-limited cluster-cluster agglomeration. For turbulent agglomeration of latex particles in stirred tanks, Selomulya et al. [58] reported values of d_f between 1.7 and 2.1 and Waldner et al. [59] reported values of d_f between 1.8 and 2.6. A log-log plot of *N* versus R_{gyr} / r_p is shown in Figure 5a at time $t = 87.5$ for both one-way and two-way coupling computations. It was found that for both methods fractal dimension values are close, with $d_f = 2.064$ for one-way coupling and $d_f = 2.118$ for two-way coupling. This value of fractal dimension for the particle agglomerates is in good agreement with values noted above obtained in previous experimental literature for turbulent agglomeration.

The fractal dimension was calculated at different time intervals during the computations. The calculated fractal dimension is plotted as a function of time and is shown in Figure 5b. The fractal dimension for one-way and two-way coupling computations is quite close; however, the result for two-way coupling is a little higher near the end of the computation (for $t > 70$). A larger value of fractal dimension for two-way coupling implies that the agglomerates were more densely packed in comparison to the one-way coupling results.

Figure 6a shows the distribution of agglomerate sizes at $t = 87.5$. The number of particles in the agglomerate is divided into a set of logarithmic bins of base 2, such that the width of each bin is twice the width of the previous bin. The *x*-axis plots the median number of particles in the bin and the *y*-axis plots the number of agglomerates falling into that bin, where both axes are logarithmic. A similar plot is shown in Figure 6b, with the difference that the agglomerate size is characterized by bins of the ratio R_{gyr} / r_p of agglomerate gyration radius to individual particle

radius. Because the values of this ratio have a narrower size variation than the number of particles in the agglomerate, the bins used in Figure 6b are linear, with a constant width. The plots in Figure 6 demonstrate that the two-way coupling computation generates larger agglomerates with more particles than does the one-way coupling computation.

The particle volume fraction ϕ_i is computed for each agglomerate by dividing the volume of all particles associated with the agglomerate, $V_p = (4\pi/3)N_i r_p^3$, by the effective volume V_{eff} occupied by the agglomerate. The agglomerate effective volume is estimated by $V_{eff} = (4\pi/3)R_{eff,i}^3$, where the effective radius of the agglomerate R_{eff} is related to the radius of gyration as $R_{gyr} = \sqrt{2/5}\, R_{eff}$. This latter expression is based on the expression for radius of gyration of a solid sphere of uniform density. The particle volume fraction of the agglomerate can be related to the fractal dimension by [2, 30]

$$\phi_i = \phi_0 (R_{gyr,i} / r_p)^{d_f - 3}, \tag{29}$$

where ϕ_0 is a constant. If $d_f < 3$, an increase in agglomerate size results in a decrease in average particle volume fraction [4]. A log-log plot of the averaged agglomerate volume fraction versus the dimensionless radius of gyration (R_{gyr}/r_p) is given in Figure 7a at time $t = 87.5$. The observed decrease in volume fraction as the agglomerate size increases is substantial. The two-way and one-way coupling results for volume fraction are fairly close for the smaller agglomerates, but for the larger agglomerates the two-way coupling simulations yield somewhat larger particle volume fraction than do the simulations with one-way coupling. This result is consistent with our previous observation that the fractal dimension for two-way coupling

simulations is slightly larger than for one-way coupling. Figure 7b shows a log-log plot of volume fraction ϕ versus R_{gyr}/r_p at time $t = 87.5$ for both one-way and two-way coupling computations. The slopes of the best-fit lines to the data were obtained as -0.9351 and -0.8818 for one-way and two-way coupling, respectively. These values almost exactly agree with the exponent $d_f - 3$ given in (29) using the previously cited values of fractal dimension d_f.

In order to better clarify the physical differences between the one-way and two-way coupling computational results, we define V_{par} and V_{rel} as the average magnitudes of the particle velocity **v** and the particle slip velocity $\mathbf{v}_{slip} = \mathbf{v} - \mathbf{u}$, respectively. The magnitudes of the particle velocity and the particle slip velocity were computed for all particles, and then averaged over all particles contained within agglomerates (omitting values for single particles that are not in an agglomerate). Time variation of both V_{par} and V_{rel} is plotted in Figure 8a for case 2. The average particle velocity magnitude V_{par} fluctuates for both the one-way and two-way coupling computations within the interval 0.35-0.45, which is slightly greater than the root-mean-square turbulence fluctuation velocity $u_0 \cong 0.285$ listed in Table 1. The average particle slip velocity V_{rel} similarly remains approximately constant in time for the one-way coupling run. For the two-way coupling case, by contrast, the value of V_{rel} is observed to gradually decrease in time, with a value at the end of the run that is nearly half of the initial value. The decrease in particle slip velocity with time for the two-way coupling computation is an indication that the fluid velocity within the agglomerate is becoming correlated with the particle velocity, resulting in a reduction of the relative velocity between the two phases within the larger agglomerates. Another measure of this phenomenon is represented by the agglomerate penetration parameter *P*, which is defined as

$$P = \frac{V_{rel}}{V_p}. \tag{30}$$

The time variation of P is plotted in Figure 8b, showing approximately constant value for one-way coupling and a steady reduction in time for the two-way coupling computation. Both the higher volume fraction of agglomerates with two-way coupling and the correlation between the fluid and particle velocity fields makes it increasingly difficult for the fluid to penetrate into the agglomerates of the two-way coupling run as the agglomerate size increases.

To further examine the spatial variation of various fields within the agglomerate, we introduce a second-moment measure $\mu_i(F)$ of a given field $F(\mathbf{x})$ for each agglomerate i as

$$\mu_i(F) = \frac{N_i \left(\sum_{j=1}^{N_i} \left| \mathbf{x}_j - \overline{\mathbf{x}}_i \right|^2 F_j \right)}{\left(\sum_{j=1}^{N_i} \left| \mathbf{x}_j - \overline{\mathbf{x}}_i \right|^2 \right) \left(\sum_{j=1}^{N_i} F_j \right)}, \tag{31}$$

where $\overline{\mathbf{x}}_i$ is the centroid of agglomerate i and F_j is the value of the function $F(\mathbf{x})$ evaluated at the centroid $\mathbf{x}_j$ of the j^{th} particle within the agglomerate. The second-moment measure is shown in Figures 9a and 9b for two different fields − the relative velocity magnitude $\left| \mathbf{v}_{slip} \right|$ and a strain rate measure $S = \sqrt{2\mathbf{D} : \mathbf{D}}$, where $\mathbf{D}$ is the fluid rate of deformation tensor. For each of these two fields, the average value of the moment $\mu_i(F)$ is plotted as a function of number of particles in the agglomerate using the same logarithmic bins as used in Figure 6a, where the averaging is performed for all agglomerates in each bin. A value of the second moment $\mu(F)$ equal to unity

indicates that the function $F(\mathbf{x})$ is uniform (or statistically randomly varying) across the agglomerate, whereas a value of $\mu_i(F)$ that is less (greater) than unity implies that particles with higher (lower) values of $F(\mathbf{x})$ are found near the center of the agglomerate compared to particles on the outer parts of the agglomerate. Obviously, for the smallest bin representing agglomerates with only two particles, all second moments are equal to unity by definition.

The second moment of the relative velocity magnitude is shown in Figure 9a. The second moment is observed to be larger than unity for both one-way and two-way coupling computations, particularly within the middle range of agglomerate size spanning from 6 to 1500 particles. The second moment for the one-way coupling computation tends to be higher in the lower end of this range, for agglomerates with between about 6 to 40 particles, and the values for the two-way coupling computation tend to be higher for the upper part of this range, for agglomerates with between 700 to 1500 particles. Several mechanisms play a role in increasing the second moment of the relative velocity above unity. A mechanism that is present for both one-way and two-way coupling computations is the rotational inertia of the particles, which leads to a particle velocity magnitude that increases linearly with distance from the agglomerate centroid. Consequently, the value of V_{rel} is higher for the outermost particles, which are a farther distance away from the agglomerate center than the innermost particles, hence causing the second moment to increase above unity. A similar linear velocity variation with distance from the centroid exists for shearing or elongational deformation of the agglomerates. For the computation with two-way coupling, the fluid within the inner region of the agglomerate is influenced by the particle-induced body force and becomes correlated to the particle velocity, such that the fluid within the agglomerate moves with the inner particles. This effect will tend to

decrease V_{rel} for the inner particles (and increase the second moment) in the two-way coupling computation, but it occurs primarily for larger agglomerates.

The second moment of the straining rate measure $S = \sqrt{2\mathbf{D} : \mathbf{D}}$ is shown in Figure 9b. The value of this measure is nearly equal to unity for the one-way coupling computation since the straining measure depends only on the fluid flow, and hence can be treated as a random variable. The second moment of the straining measure is also close to unity for small agglomerates with two-way coupling. As the number of particles per agglomerate increases (to a value greater than about 100), the straining rate measure gradually increases above unity, indicating that the straining rate experienced by the particles is higher for particles near the outer edges of the agglomerate than for particles near the center. The outermost particles can act almost like a screen for the larger agglomerates with two-way coupling, preventing the inner particles from being exposed to high strain rate. This observation is consistent with the results of studies, such as Binder et al. [60] or Fellay et al. [61], that use direct simulation techniques such as lattice-Boltzmann or Stokesian dynamics to compute simple flow fields or rotational motion for single agglomerate structures. For larger-size agglomerates that are nearly spherical in shape, our findings are also approximately consistent with the shell-core model for agglomerate structure proposed by Kusters et al. [30], in which each agglomerate is idealized as a two-layer sphere, where the outer 'shell' layer is porous and the inner 'core' layer is impermeable.

There is, of course, some inaccuracy in the second moment measure discussed above, since the agglomerates are not particularly spherical in shape, but instead appear to have a wide variety of jagged and/or elongated shapes. To make the relative velocity and strain rate measures more understandable, we have visualized the relative velocity and strain rate measures for some sample agglomerates from the two-way coupling computation in Figures 10a and 10b. These

figures visually confirm that outer regions of the agglomerates experience higher values of the relative velocity and shear measures compared to points in the inner region of the agglomerates, even for non-spherical agglomerates.

4. Conclusions

A series of computations were performed to examine the differences between computations of turbulent particle agglomeration with one-way and with two-way phase coupling. The computations examined cases with Kolmogorov-scale Stokes numbers varying from about 0.8 to about 14. In agreement with previous literature examining turbulence modulation by particles in this range of Stokes numbers, we observe that the particles cause enhanced attenuation of the turbulent kinetic energy compared to computations with no particles. The rate of attenuation increased with increase in the particle size and mass loading. In a series of computations repeated both with adhesion and without adhesion, we observe little difference in the rate of particle attenuation, except for the largest size particles. Examination of the agglomeration process indicates that significant agglomeration occurred during the computations, but without any significant influence on the turbulence modulation. This observation reinforces the notion expressed in previous literature [51] that the turbulence attenuation in this Stokes number regime is dominated by particle inertia.

Examination of agglomerate structure during the turbulent agglomeration process indicated that agglomerates formed with two-way coupling were larger and contained more particles than those generated under one-way coupling computations, even though at the time of comparison the turbulent kinetic energy for the two cases was about the same. Agglomerates formed with both one-way and two-way coupling computations had about the same fractal

dimension d_f, which compared well with values cited in previous experimental literature for turbulent agglomeration. The volume concentration of particles in each agglomerate was computed and found to vary as a power function with exponent equal to $3-d_f$, in agreement with previous literature on agglomerate fractal structure [2]. While the magnitude of the particle velocity is similar for agglomerates computed with one-way and two-way coupling, the relative velocity between the particle and the fluid is much lower for the two-way coupling computations, particularly once larger-size agglomerates start to form. Several different measures indicated that the fluid flow generated in agglomerates acts to shield the inner-most particles, so that the highest shear stresses and relative velocity occurs for the outer particles in agglomerate. The motion of fluid inside the large agglomerates was found to be highly correlated to the agglomerate motion.

Acknowledgement

This research was supported by the U.S. National Science Foundation under grant CBET-1332472.

References

[1] J. Liu, W.Y. Shih, M. Sarikaya, I.A. Aksay, Fractal colloidal aggregates with finite interparticle interactions: energy dependence of the fractal dimension, Physical Review A 41(6) (1990) 3206-3213.

[2] Q. Jiang, B.E. Logan, Fractal dimensions of aggregates determined from steady-state size distributions, Environmental Science and Technology 25 (1991) 2031-2038.

[3] Y. Adachi and S. Ooi, Geometrical structure of a floc, Journal of Colloid and Interface Science 135(2) (1990) 374-384.

[4] J.S. Olfert, J.P.R. Symonds, N. Collings, The effective density and fractal dimension of particles emitted from a light-duty vehicle with a diesel oxidation catalyst, Journal of Aerosol Science 38 (2007) 69-82.

[5] A.M. Brasil, T.L. Farias, M.G. Carvalho, U.O. Koylu, Numerical characterization of the morphology of aggregated particles, Journal of Aerosol Science 32 (2001) 489-508.

[6] W.H. Shih, W.Y. Shih, S.I. Kim, J. Liu, I.A. Aksay, Scaling behavior of the elastic properties of colloidal gels, Physical Review A 42(8) (1990) 4772-4780.

[7] S.S. Narine, A.G. Marangoni, A.G., Fractal nature of fat crystal networks, Physical Review E 59(2) (1999) 1908-1920.

[8] S.S. Narine, A.G. Marangoni, Mechanical and structural model of fractal networks of fat crystals at low deformations, Physical Review E 60(6) (1999) 6991-7000.

[9] D.H. Bache, Floc rupture and turbulence: a framework for analysis, Chemical Engineering Science 59 (2004) 2521-2532.

[10] M. Kobayashi, Y. Adachi, S. Ooi, Breakup of fractal flocs in a turbulent flow, Langmuir 15 (1999) 4351-4356.

[11] K. Higashitani, K. Iimura, H. Sanda, Simulation of deformation and breakup of large aggregates in flows of viscous fluids, Chemical Engineering Science 56 (2001) 2927-2938.

[12] A. Scurati, D.L. Feke, I. Manas-Zloczower, Analysis of the kinetics of agglomerate erosion in simple shear flows, Chemical Engineering Science 60 (2005) 6564-6573.

[13] R. Wengeler, H. Nirschl, Turbulent hydrodynamic stress induced dispersion and fragmentation of nanoscale agglomerates, Journal of Colloid and Interface Science 306, (2007) 262-273.

[14] B.K. Brunk, D.L. Koch, L.W. Lion, Hydrodynamic pair diffusion in isotropic random velocity fields with application to turbulent coagulation, Physics of Fluids 9 (1997) 2670-2691.

[15] B.K. Brunk, D.L. Koch, L.W. Lion, Turbulent coagulation of colloidal particles, Journal of Fluid Mechanics 364 (1998) 81-113.

[16] B.K. Brunk, D.L. Koch, L.W. Lion, Observations of coagulation in isotropic turbulence. Journal of Fluid Mechanics 371 (1998) 81-107.

[17] J. Chun, D.L. Koch, Coagulation of monodisperse aerosol particles by isotropic turbulence, Physics of Fluids 17 (2005) 027102.

[18] D.L. Koch, S.B. Pope, Coagulation-induced particle-concentration fluctuations in homogeneous, isotropic turbulence, Physics of Fluids 14 (2002) 2447-2455.

[19] L.P. Wang, A.S. Wexler, Y. Zhou, Statistical mechanical descriptions of turbulent coagulation, Physics of Fluids 10 (1998) 2647-2651.

[20] P. Duru, D.L. Koch, C. Cohen, Experimental study of turbulent-induced coalescence in aerosols, International Journal of Multiphase Flow 33 (2007) 987-1005.

[21] W.C. Reade, L.R. Collins, L.R., A numerical study of the particle size distribution of an aerosol undergoing turbulent coagulation, Journal of Fluid Mechanics 415 (2000) 45-64.

[22] C.T. Crowe, On models for turbulence modulation in fluid-particulate flows, International Journal of Multiphase Flows 26 (2000) 719-727.

[23] J.K. Eaton, Two-way coupled turbulence simulations of gas-particle flows using point-particle tracking, International Journal of Multiphase Flow 35 (2009) 792-800.

[24] A. Saber, T.S. Lundström, J.G. Hellström, Turbulent modulation in particulate flow: a review of critical variables, Engineering 7 (2015) 597-609.

[25] C. Poelma, G. Ooms, Particle-turbulence interaction in a homogeneous, isotropic turbulent suspension, Applied Mechanics Reviews 59 (2006) 78-90.

[26] A. Rao, J.S. Curtis, B.C. Hancock, C. Wassgren, Simulation of dilute turbulent gas-particle flow with turbulence modulation, AIChE Journal 58 (2012) 1381-1396.

[27] S. Balachandar, J.K. Eaton, Turbulent dispersed multiphase flow, Annual Review of Fluid Mechanics 42 (2010) 111-133.

[28] H. Nasr, G. Ahmadi, The effect of two-way coupling and inter-particle collisions on turbulence modulation in a vertical channel flow, International Journal of Heat and Fluid Flow 28 (2007) 1507-1517.

[29] H. Rumpf, The strength of granules and agglomerates, in: W.A. Knepper (Ed.) Agglomeration, John Wiley, New York, 1962, pp. 379-418.

[30] K.A. Kusters, J.G. Wijers, D. Thoenes, Aggregated kinetics of small particles in agitates vessels, Chemical Engineering Science 52(1) (1997) 107-121.

[31] P. Vainshtein, M. Shapiro, Porous agglomerates in the general linear flow field, Journal of Colloid and Interface Science 298 (2006) 183-191.

[32] S. Hansen, D.V. Khakhar, J.M. Ottino, Dispersion of solids in nonhomogeneous viscous flows, Chemical Engineering Science 53(10) (1998) 1803-1817.

[33] J.S. Marshall, Discrete-element modeling of particulate aerosol flows, Journal of Computational Physics 228 (2009) 1541-1561.

[34] T. Bosse, L. Kleiser, C. Härtel, E. Meiburg, Numerical simulation of finite Reynolds number suspension drops settling under gravity, Physics of Fluids 17 (2005) 037101.

[35] R. Di Felice, The voidage function for fluid-particle interaction systems, International Journal of Multiphase Flow 20 (1994) 153-159.

[36] C.Y. Wen, Y.H. Yu, Mechanics of fluidization, Chemical Engineering Progress Symposium Series 62(62) (1966) 100-111.

[37] C.T. Crowe, J.D. Schwarzkopf, M. Sommerfeld, Y. Tsuji, Multiphase Flows with Droplets and Particles, second ed., CRC Press, Boca Raton, Florida, 2012.

[38] P.G. Saffman, The lift on a small sphere in a slow shear flow, Journal of Fluid Mechanics 22 (1965) 385-400.

[39] S.I. Rubinow, J.B. Keller, The transverse force on a spinning sphere moving in a viscous fluid, Journal of Fluid Mechanics 11 (1961) 447-459.

[40] K.L. Johnson, K. Kendall, A.D. Roberts, Surface energy and the contact of elastic solids, Proceedings of the Royal Society of London A 324 (1971) 301-313.

[41] A. Chokshi, A.G.G.M. Tielens, D. Hollenbach, Dust coagulation, The Astrophysical Journal 407 (1993) 806-819.

[42] G.G. Joseph, R. Zenit, M.L. Hunt, A.M. Rosenwinkel, Particle-wall collisions in a viscous fluid, Journal of Fluid Mechanics 433 (2001) 329-346.

[43] Y. Tsuji, T. Tanaka, T. Ishida, Lagrangian numerical simulation of plug flow of cohesionless particles in a horizontal pipe, Powder Technology 71 (1992) 239-250.

[44] K. Bagi, M.R. Kuhn, A definition of particle rolling in a granular assembly in terms of particle translations and rotations, Journal of Applied Mechanics 71 (2004) 493-501.

[45] C. Dominik, A.G.G.M. Tielens, Resistance to rolling in the adhesive contact of two elastic spheres, Philosophical Magazine A 92(3) (1995) 783-803.

[46] A. Vincent, M. Meneguzzi, The spatial structure and statistical properties of homogeneous turbulence, Journal of Fluid Mechanics 225 (1991) 1-20.

[47] T.S. Lundgren, Linearly forced isotropic turbulence, Annual Research Briefs, CTR, Stanford, 2003, pp. 461-473.

[48] C. Rosales, C. Meneveau, Linear forcing in numerical simulations of isotropic turbulence: physical space implementations and convergence properties, Physics of Fluids 17(9) (2005) 095106.

[49] J.S. Marshall, S. Li, Adhesive Particle Flow: A Discrete Element Approach, Cambridge University Press, New York, 2014.

[50] O.A. Druzhinin, S.E. Elghobashi, On the decay rate of isotropic turbulence laden with microparticles, Physics of Fluids 11 (1999) 602-610.

[51] O.A. Druzhinin, The influence of particle inertia on the two-way coupling and modification of isotropic turbulence by microparticles, Physics of Fluids 13(12) (2001) 3738-3755.

[52] K.D. Squires, J.K. Eaton, Particle response and turbulence modification in isotropic turbulence, Physics of Fluids A 2 (1990) 1191-1203.

[53] M. Boivin, O. Simonin, K.D. Squires, Direct numerical simulation of turbulence modulation by particles in isotropic turbulence, Journal of Fluid Mechanics 375 (1998) 235-263.

[54] S.E. Elghobashi, G.C. Truesdell, On the two-way interaction between homogeneous turbulence and dispersed solid particles. I. Turbulence modification, Physics of Fluids A 5 (1993) 1790-1801.

[55] S. Sundaram, L.R. Collins, A numerical study of the modulation of isotropic turbulence by suspended particles, Journal of Fluid Mechanics 379 (1999) 105-143.

[56] R.A. Gore, C.T. Crowe, The effect of particle size on modulating turbulent intensity, International Journal of Multiphase Flow 15 (1989) 279-285.

[57] M.L. Eggersdorfer, D. Kadau, H.J. Hermann, S.E. Pratsinis, Multiparticle sintering dynamics: From fractal-like aggregates to compact structures, Langmuir 27 (2011) 6358-6367.

[58] C. Selomulya, R. Amal, G. Bushell, T.D. Waite, Evidence of shear rate dependence on restructuring and breakup of latex aggregates, Journal of Colloid and Interface Science 236 (2001) 67-77.

[59] M.H. Waldner, J. Sefcik, M. Soos, M. Morbidelli, Initial growth kinetics of aggregates in turbulent coagulator, Powder Technology 156 (2005) 226-234.

[60] C. Binder, C. Feichtinger, H.-J. Schmid, N. Thürey, W. Peukert, U. Rüde, Simulation of the hydrodynamic drag of aggregated particles, Journal of Colloid and Interface Science 301 (2006) 155-167.

[61] L.S. Fellay, C. Twist, M. Vanni, Motion of rigid aggregates under different flow conditions, Acta Mechanica 224 (2013) 2225-2248.

Figure Captions

Figure 1. Time variation of (a) turbulent kinetic energy q and (b) turbulence dissipation rate ε, with results from computations with one-way coupling (dashed line, deltas) and two-way coupling (solid line, circles).

Figure 2. (a) Power spectrum for computation with two-way coupling for case 2 at three different times: t = 0 (black line), 50 (blue line) and 87.5 (red line). (b) Power spectrum for computations with Kolmogorov-scale Stokes numbers $\mathrm{St}_K = 0.86$ (black), 3.44 (blue), 7.74 (red), and 13.8 (green) at $t = 87.5$ both with adhesion (Ad_0 = 12.3, cases 1-4)(solid lines) and without adhesion (Ad_0 = 0, cases 5-8)(dashed lines).

Figure 3. Plots showing (a) the number of particles per agglomerate N_{pagg} and (b) the dimensionless particle-weighted average radius of gyration, $\overline{R}_{gyr}/r_p$, as a function of integral-scale adhesion parameter, Ad_0, for computations with two-way coupling (solid lines, circles) and one-way coupling (dashed lines, deltas) at time $t = 87.5$. Computations are for cases 2 and 9-12.

Figure 4. Time variation of (a) the total number of agglomerates (N_{agg}) and (b) the average number of particles per agglomerate (N_{pagg}) and (c) the dimensionless particle-weighted radius of gyration of agglomerates ($\overline{R}_{gyr}/r_p$) with results from computations with one-way coupling (dashed lines) and two-way coupling (solid lines) for case 2.

Figure 5. (a) Plot showing power-law fit given in Eq. (28) between the number of particles in an agglomerate N, versus the ratio of the gyration radius to the primitive particle radius, R_{gyr}/r_p. Slope of lines on the log-log plot are equal to the fractal dimension d_f at $t = 87.5$, and results are given for both one-way coupling (blue crosses) and two-way coupling (red circles). (b) Plot showing time variation of the fractal dimension, comparing results with one-way coupling (dashed line, deltas) and two-way coupling (solid line, circles) for case 2.

Figure 6. Distribution plots showing number of agglomerates N_{agg} as a function of (a) number of particles in the agglomerate averaged over a set of logarithmic bins, N_B, and (b) dimensionless radius of gyration, R_{gyr}/r_p, averaged over a set of linear bins. Results are from computations with one-way coupling (A, blue bars) and two-way coupling (B, red bars) at t = 87.5 for case 2.

Figure 7. (a) Distribution plot showing the particle volume fraction as a function of the dimensionless radius of gyration, R_{gyr}/r_p, on a log-linear plot for both one-way coupling (blue bars) and two-way coupling (red bars). (b) Plot showing the power-law fit given in Eq. (29), where the slope of lines on the log-log plot are equal to the fractal dimension $d_f - 3$. The data is for case 2 at $t = 87.5$, for one-way coupling (blue crosses) and two-way coupling (red circles).

Figure 8. Time variation of (a) the average particle velocity magnitude V_{par} (upper curves) and the average particle slip velocity magnitude V_{rel} (lower curves) and (b) the agglomerate flow penetration parameter P for computations with one-way (dashed lines, deltas) and two-way (solid lines, circles) coupling for case 2.

Figure 9. Second-order moment plots for (a) relative velocity magnitude V_{rel}, and (b) shear measure $S = \sqrt{2\mathbf{D} : \mathbf{D}}$, shown for results of computations with one-way coupling (blue bars) and two-way coupling (red bars) for case 2 at $t = 87.5$. The number of particles in the agglomerate are grouped logarithmically into bins, with average number of particles for the given bin indicated by N_B.

Figure 10. Scatter plots of the five largest agglomerates with colors indicating (a) the relative velocity magnitude and (b) the shear stress measure S for the two-way coupling run for case 2 at $t = 100$.

Table 1. Dimensionless simulation parameters and physical parameters of the fluid turbulence.

Simulation Parameters		**Turbulence Parameters**	
Time step	0.002	Turbulent kinetic energy, q	0.122
Cycles	15000	Mean dissipation rate, ε	0.015
Grid	128^3	Kinematic viscosity, ν	0.001
		Integral length, ℓ_0	0.771
		Taylor microscale, λ	0.285
		Kolmogorov length, η	0.016
		Integral velocity, u_0	0.285
		Integral time, T_ℓ	2.71

Table 2. List of computational cases examined. For each case computations were performed with and without two-way coupling. Variables listed include ratio of particle radius to integral length scale, average particle volume concentration $\bar{\phi}$, mass loading Z, Kolmogorov and integral scale Stokes number, and Kolmogorov and integral scale adhesion parameter.

Case	r_p / ℓ_0	$\bar{\phi}$	Z	$\mathrm{St_K}$	$\mathrm{St_0}$	$\mathrm{Ad_K}$	$\mathrm{Ad_0}$
1	0.0129	0.000788	0.00789	0.860	0.082	260	12.3
2	0.0259	0.0063	0.0634	3.44	0.328	260	12.3
3	0.0389	0.0213	0.218	7.74	0.738	260	12.3
4	0.0516	0.0504	0.531	13.8	1.31	260	12.3
5	0.0129	0.000788	0.00789	0.860	0.082	0	0
6	0.0259	0.0063	0.0634	3.44	0.328	0	0
7	0.0389	0.0213	0.218	7.74	0.738	0	0
8	0.0516	0.0504	0.531	13.8	1.31	0	0
9	0.0259	0.0063	0.0634	3.44	0.328	130	6.16
10	0.0259	0.0063	0.0634	3.44	0.328	520	24.6
11	0.0259	0.0063	0.0634	3.44	0.328	1041	49.3
12	0.0259	0.0063	0.0634	3.44	0.328	2081	98.5

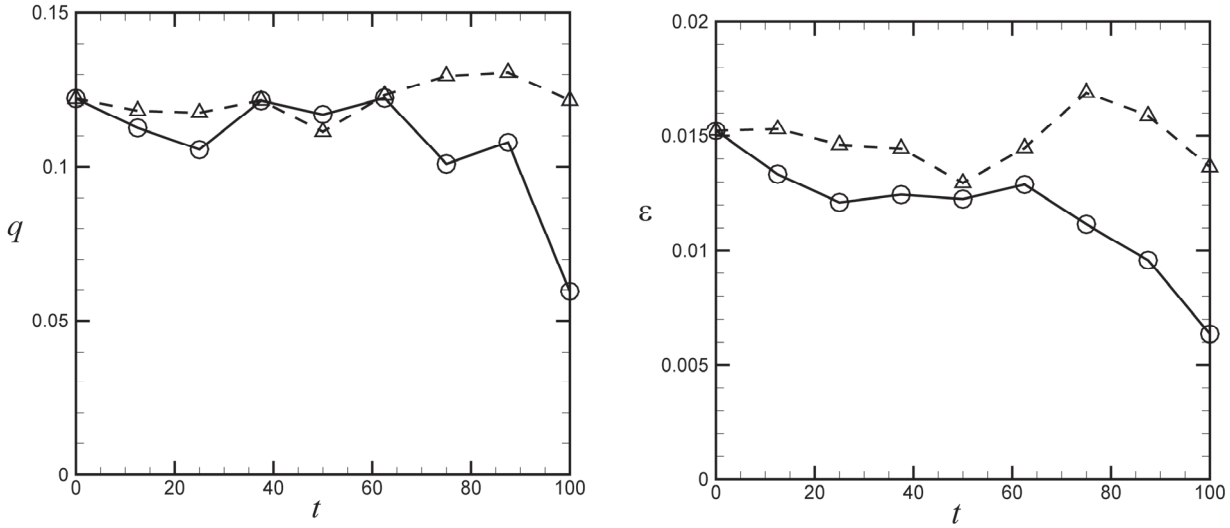

(a) (b)

Figure 1. Time variation of (a) turbulent kinetic energy q and (b) turbulence dissipation rate ε, with results from computations with one-way coupling (dashed line, deltas) and two-way coupling (solid line, circles).

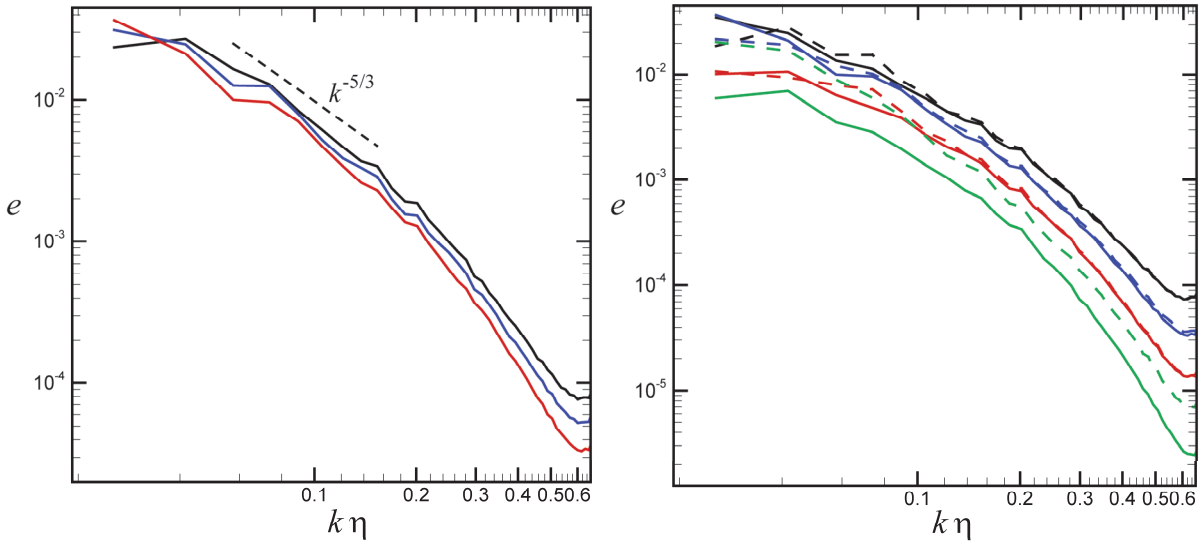

(a) (b)

Figure 2. (a) Power spectrum for computation with two-way coupling for case 2 at three different times: $t = 0$ (black line), 50 (blue line) and 87.5 (red line). (b) Power spectrum for computations with Kolmogorov-scale Stokes numbers $\mathrm{St}_K = 0.86$ (black), 3.44 (blue), 7.74 (red), and 13.8 (green) at $t = 87.5$ both with adhesion ($\mathrm{Ad}_0 = 12.3$, cases 1-4)(solid lines) and without adhesion ($\mathrm{Ad}_0 = 0$, cases 5-8)(dashed lines).

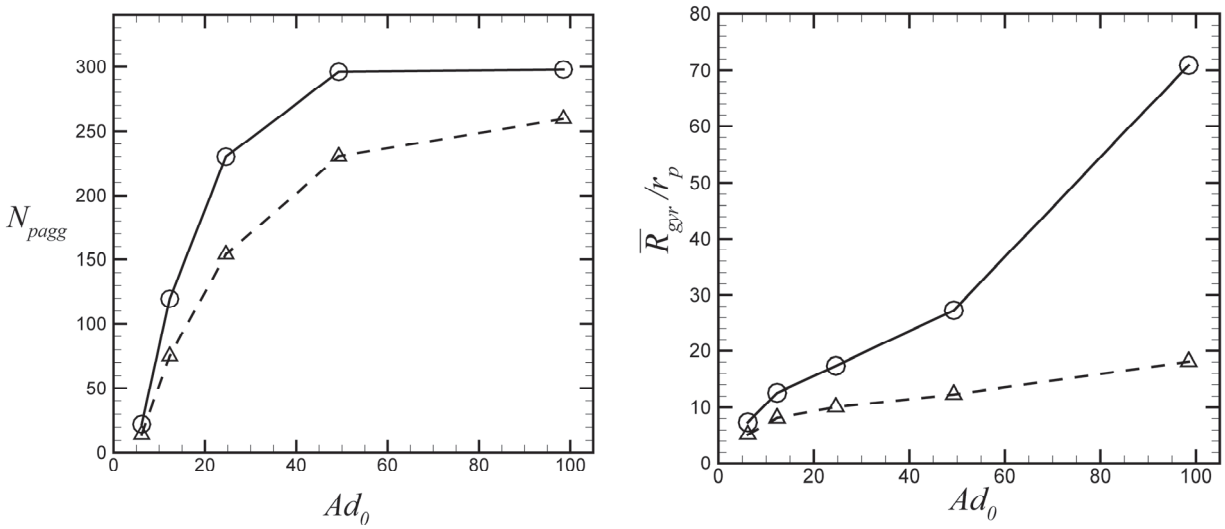

Figure 3. Plots showing (a) the number of particles per agglomerate N_{pagg} and (b) the dimensionless particle-weighted average radius of gyration, $\overline{R}_{gyr}/r_p$, as a function of integral-scale adhesion parameter, Ad_0, for computations with two-way coupling (solid lines, circles) and one-way coupling (dashed lines, deltas) at time $t = 87.5$. Computations are for cases 2 and 9-12.

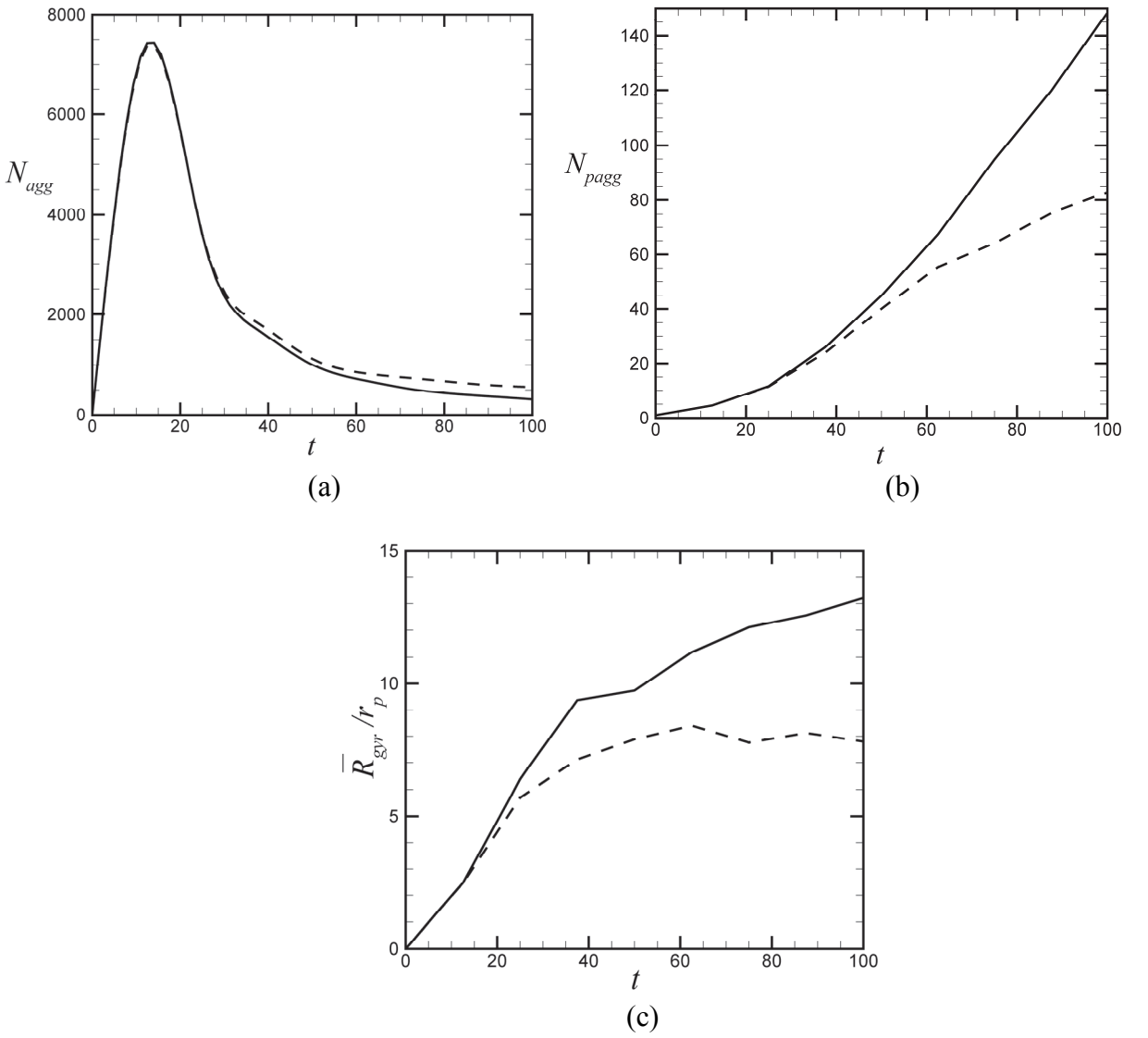

Figure 4. Time variation of (a) the total number of agglomerates (N_{agg}) and (b) the average number of particles per agglomerate (N_{pagg}) and (c) the dimensionless particle-weighted radius of gyration of agglomerates ($\overline{R}_{gyr}/r_p$) with results from computations with one-way coupling (dashed lines) and two-way coupling (solid lines) for case 2.

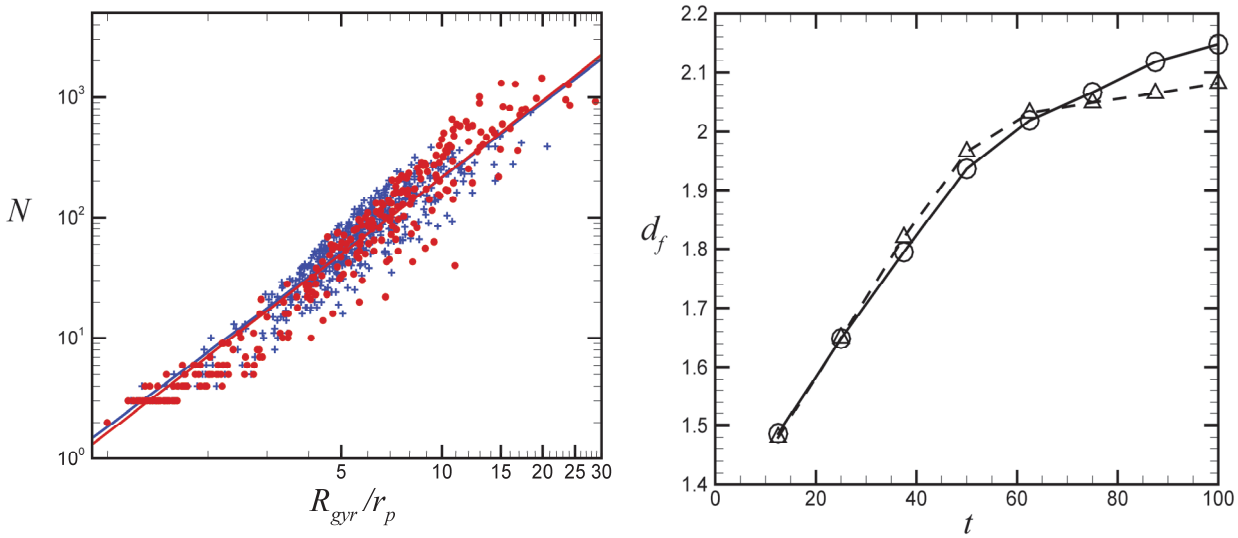

Figure 5. (a) Plot showing power-law fit given in Eq. (28) between the number of particles in an agglomerate N, versus the ratio of the gyration radius to the primitive particle radius, R_{gyr}/r_p. Slope of lines on the log-log plot are equal to the fractal dimension d_f at $t = 87.5$, and results are given for both one-way coupling (blue crosses) and two-way coupling (red circles). (b) Plot showing time variation of the fractal dimension, comparing results with one-way coupling (dashed line, deltas) and two-way coupling (solid line, circles) for case 2.

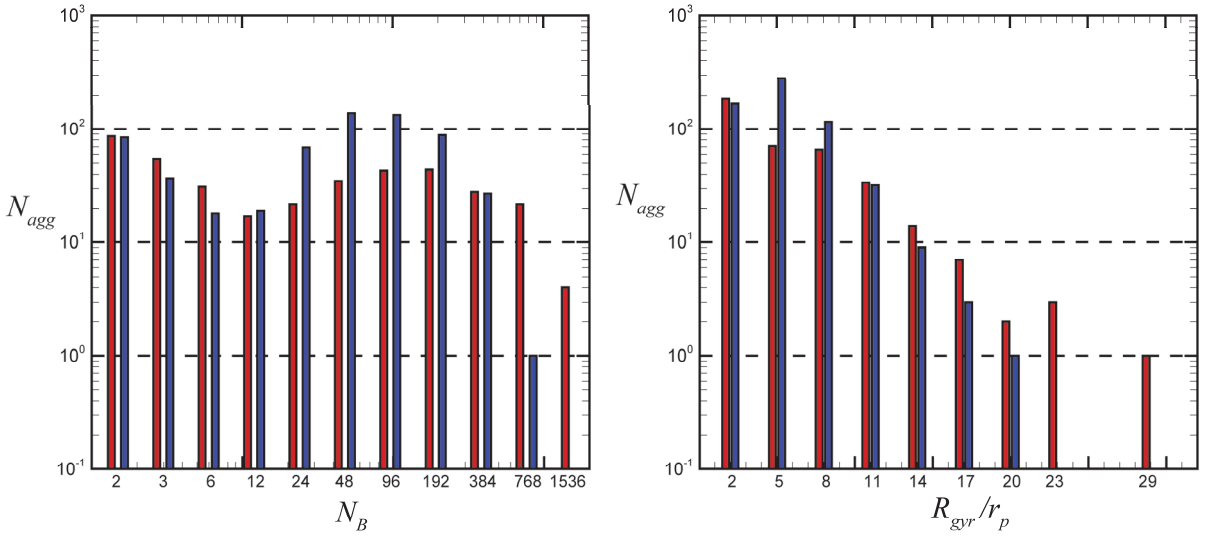

Figure 6. Distribution plots showing number of agglomerates N_{agg} as a function of (a) number of particles in the agglomerate averaged over a set of logarithmic bins, N_B, and (b) dimensionless radius of gyration, R_{gyr}/r_p, averaged over a set of linear bins. Results are from computations with one-way coupling (A, blue bars) and two-way coupling (B, red bars) at t = 87.5 for case 2.

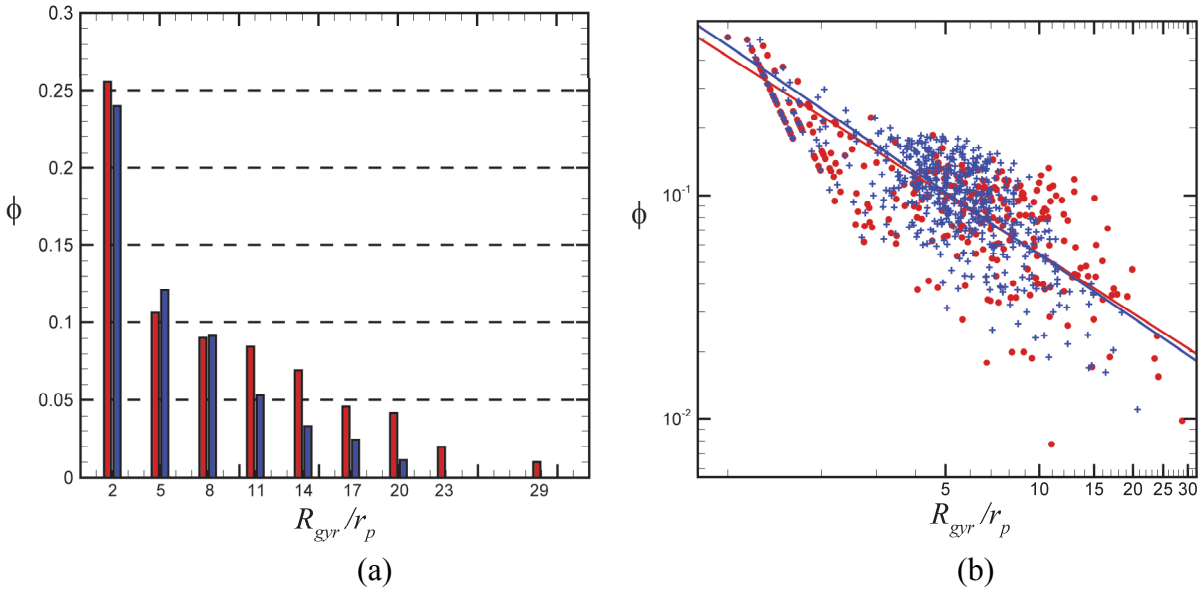

Figure 7. (a) Distribution plot showing the particle volume fraction as a function of the dimensionless radius of gyration, R_{gyr}/r_p, on a log-linear plot for both one-way coupling (blue bars) and two-way coupling (red bars). (b) Plot showing the power-law fit given in Eq. (29), where the slope of lines on the log-log plot are equal to the fractal dimension $d_f - 3$. The data is for case 2 at $t = 87.5$, for one-way coupling (blue crosses) and two-way coupling (red circles).

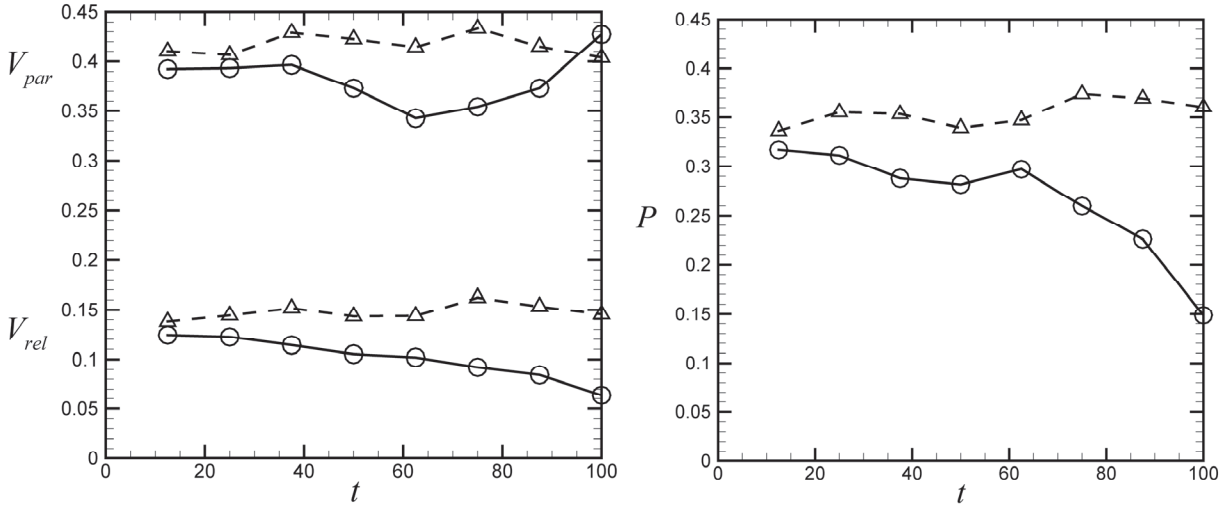

(a) (b)

Figure 8. Time variation of (a) the average particle velocity magnitude V_{par} (upper curves) and the average particle slip velocity magnitude V_{rel} (lower curves) and (b) the agglomerate flow penetration parameter P for computations with one-way (dashed lines, deltas) and two-way (solid lines, circles) coupling for case 2.

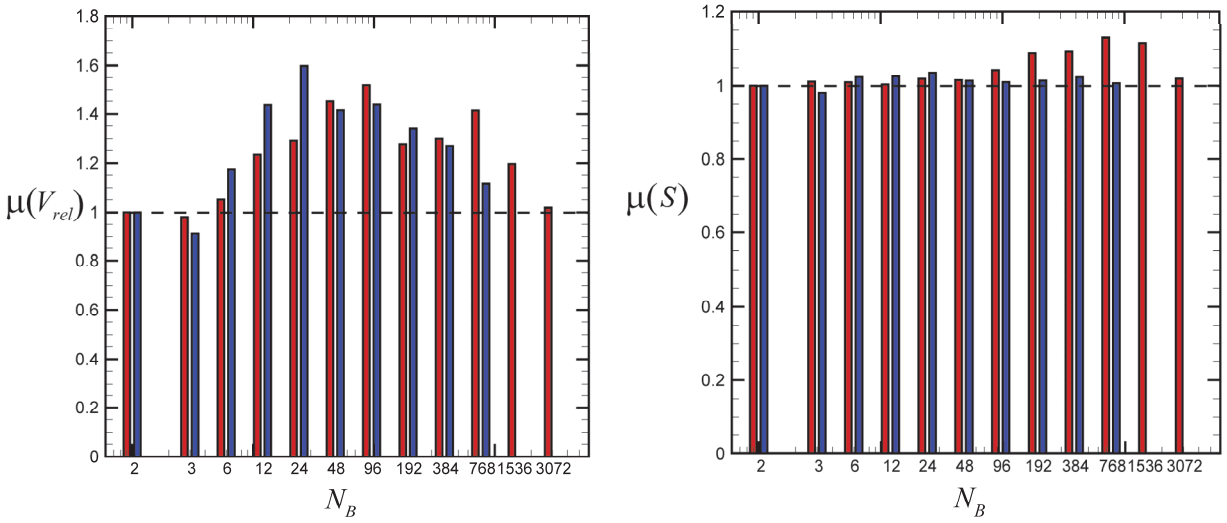

Figure 9. Second-order moment plots for (a) relative velocity magnitude V_{rel}, and (b) shear measure $S = \sqrt{2\mathbf{D} : \mathbf{D}}$, shown for results of computations with one-way coupling (blue bars) and two-way coupling (red bars) for case 2 at $t = 87.5$. The number of particles in the agglomerate are grouped logarithmically into bins, with average number of particles for the given bin indicated by N_B.

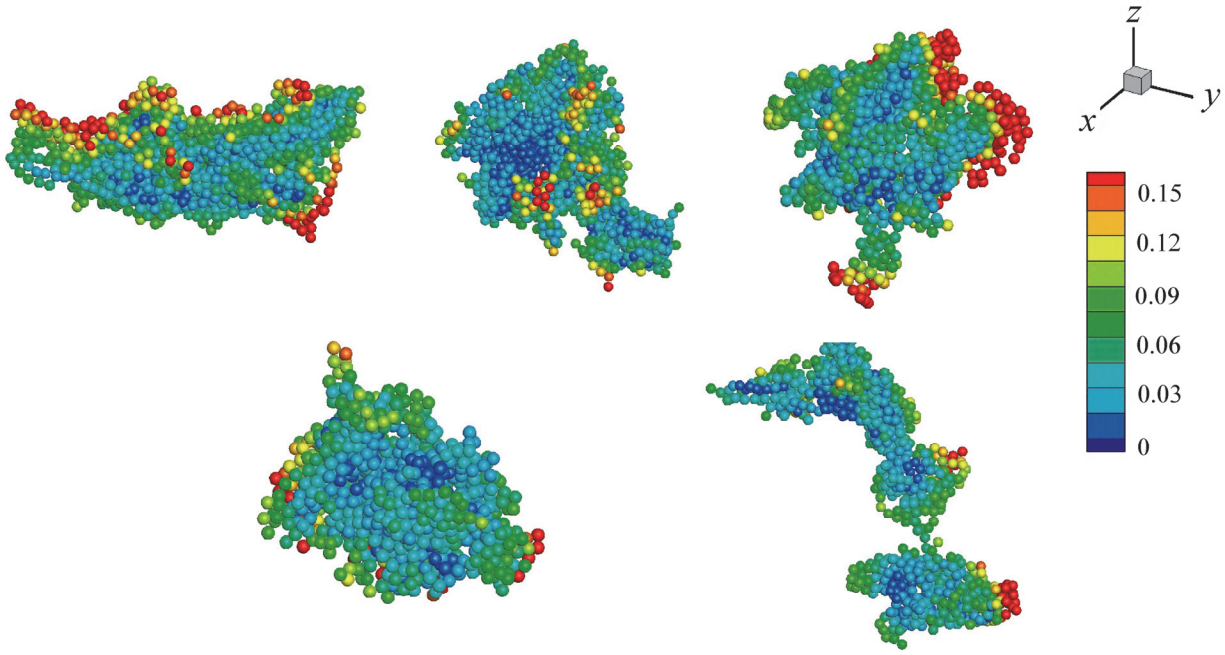

(a)

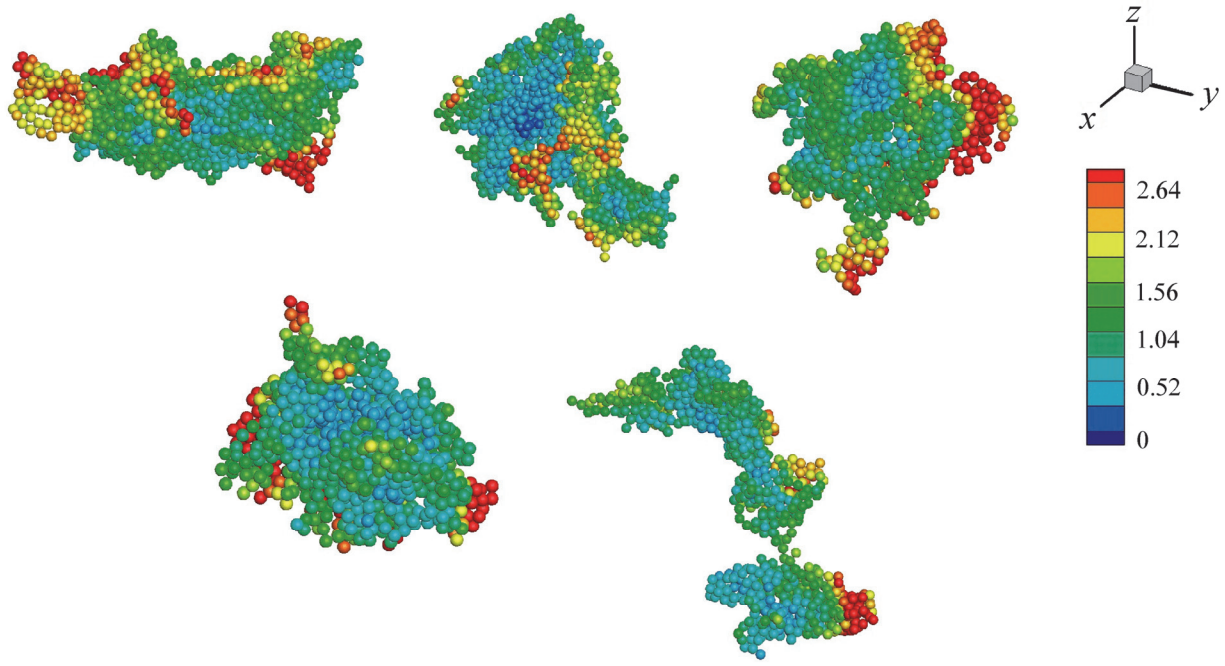

(b)

Figure 10. Scatter plots of the five largest agglomerates with colors indicating (a) the relative velocity magnitude and (b) the shear stress measure S for the two-way coupling run for case 2 at $t = 100$.